

SCIENTIFIC REPORTS



OPEN

NEMS With Broken T Symmetry: Graphene Based Unidirectional Acoustic Transmission Lines

Mehdi B. Zanjani¹, Arthur R. Davoyan², Nader Engheta² & Jennifer R. Lukes¹

Received: 19 December 2014

Accepted: 20 March 2015

Published: 20 May 2015

In this work we discuss the idea of one-way acoustic signal isolation in low dimensional nanoelectromechanical oscillators. We report a theoretical study showing that one-way conversion between in-phase and anti-phase vibrational modes of a double layer graphene nanoribbon is achieved by introducing spatio-temporal modulation of system properties. The required modulation length in order to reach full conversion between the two modes is subsequently calculated. Generalization of the method beyond graphene nanoribbons and realization of a NEMS signal isolator are also discussed.

Low dimensional materials such as graphene^{1–4}, carbon nanotubes⁵, boron nitride nanomaterials^{6–9}, and atomically thin MoS₂¹⁰ have attracted great interest in recent years. The extraordinary electrical^{11,12}, optical^{13,14}, thermal^{15,16}, and mechanical^{17,18} properties of graphene and analogous low-dimensional materials¹⁹ make them promising candidates for practical applications in electronics, sensing, and energy storage devices.

Owing to their outstanding mechanical and electrical properties, these materials have been utilized as electromechanical oscillators in nanoscale memory cells and nanoelectromechanical switches^{20–23} and resonators^{24–26}. The study of mechanical waves²⁷ and the ability to manipulate, control, and detect vibrational motion in such nanoelectromechanical systems (NEMS)^{28–31} provides unprecedented opportunities to employ them in fluidic³², electronic³³, and optical networks³⁴. NEMS based oscillators as mechanical sensors and actuators are also used in applications such as ultrasensitive force³⁵ and displacement detection^{36,37}, scanning probe microscopy³⁸ and resonant mass sensing of chemical and biological species^{39,40} where an important functionality is to have one-way communication channels that transmit desired signals only in one direction.

Acoustic rectifiers and diodes^{41–45} as well as one-way acoustic isolators⁴⁶ have been recently studied. The acoustic diode concept is based on a nonlinear frequency conversion mechanism^{44,47,48}. Other studies have focused on nonreciprocity in acoustic circulators and acoustic metamaterials^{49,50} as well as optomechanically induced nonreciprocity in resonators^{51,52}. More recently, the idea of one-way phonon isolation⁴⁶, motivated by optical equivalents^{53,54}, was studied based on creating spatio-temporal modulation of mechanical properties. This leads to a one-way conversion between the guided modes, therefore breaking the symmetry of wave propagation in a waveguide in forward and backward directions.

In this letter we study the idea of one-way signal isolation in low dimensional nanoelectromechanical oscillators where the symmetry of the system under time reversal transformation, also known as the T-symmetry, is broken. To explain the method, we consider a system of graphene nanoribbons (GNRs) on an elastic substrate and demonstrate that the symmetry of wave propagation may be broken by introducing spatial and temporal modulation of elastic properties of the system. We show, both analytically and numerically, that in one of the propagation directions conversion between the modes occurs, whereas in the other direction the signal is transmitted without any perturbations. We also discuss the

¹Department of Mechanical Engineering and Applied Mechanics, University of Pennsylvania, Philadelphia, PA 19104, USA. ²Department of Electrical and Systems Engineering, University of Pennsylvania, Philadelphia, PA 19104, USA. Correspondence and requests for materials should be addressed to J.R.L. (email: jrlukes@seas.upenn.edu)

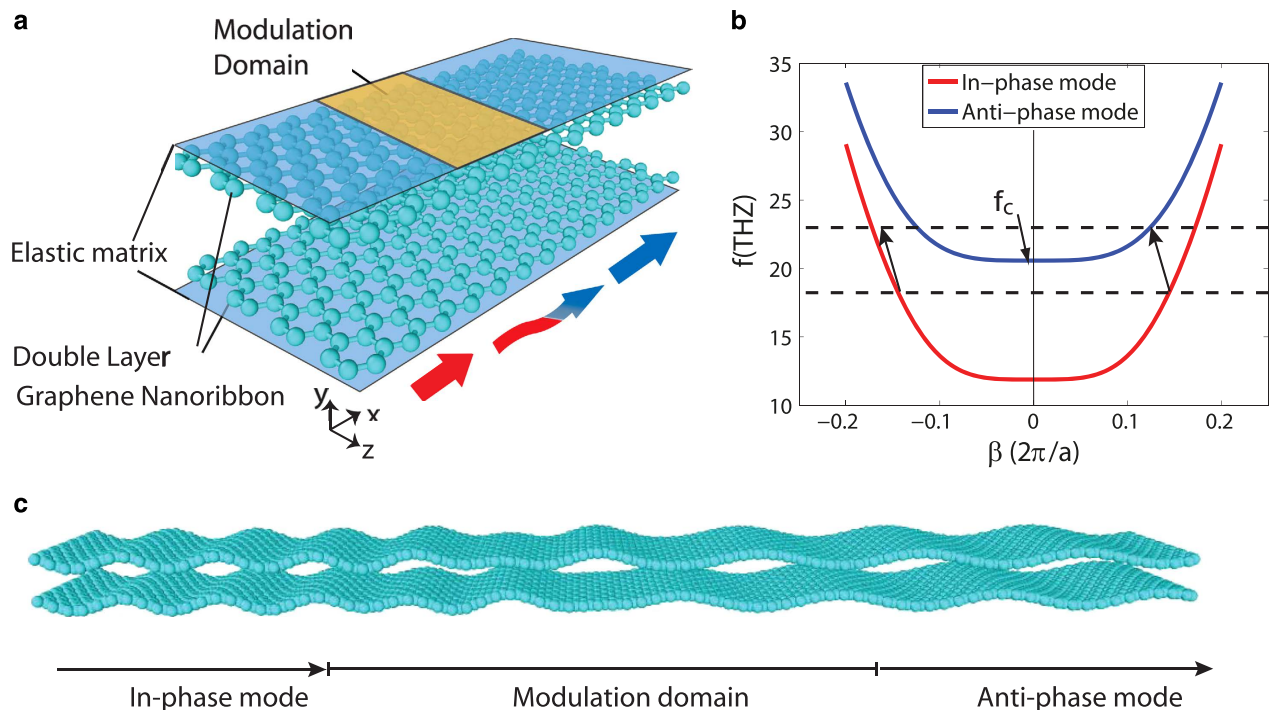


Figure 1. (a) A double-layer graphene nanoribbon on an elastic matrix. (b) Dispersion curve of the double-layer GNR obtained from Euler-Bernoulli beam model. The red and blue curves belong to the in-phase and anti-phase flexural modes, respectively. (c) Schematic of in-phase to anti-phase mode conversion in a double-layer GNR system.

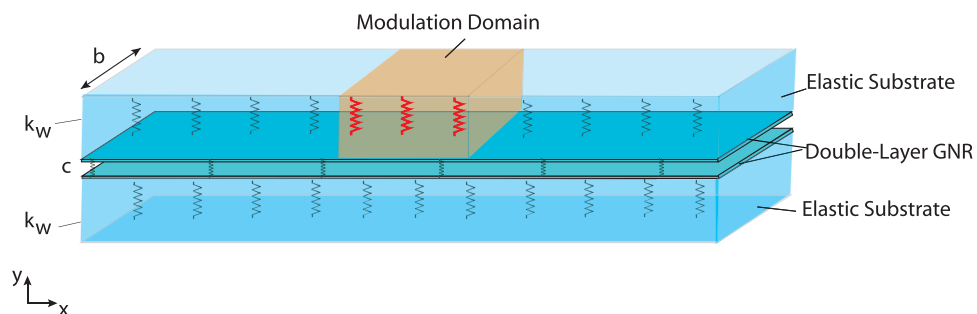


Figure 2. Schematic of continuum beam model for double-layer GNR on an elastic substrate with stiffness k_w . The shaded area represents the modulation domain.

extension of this method beyond graphene nanoribbons and mention its possible implementation for designing a phonon isolator in nanoelectromechanical oscillators.

In Fig. 1(a), a double-layer graphene nanoribbon is shown. The system consists of two graphene nanoribbons with width b , each of which is perfectly adhered to an elastic substrate. We use nonlocal elasticity theory to study wave propagation along the nanoribbons^{55,56}. In this model, shown in Fig. 2, each substrate is treated as a linear elastic medium with stiffness k_w ⁵⁶, and the nanoribbons themselves interact via van der Waals forces that are also modeled as linear springs with stiffness c ⁵⁶. The governing equation for wave propagation in this system is driven from the nonlocal Euler-Bernoulli beam model^{57,58},

$$EI \frac{\partial^4 w_1}{\partial x^4} + \rho A \frac{\partial^2}{\partial t^2} (w_1 - (e_0 a)^2 \frac{\partial^2 w_1}{\partial x^2}) = c(w_2 - w_1) - k_w w_1 \quad (1)$$

$$EI \frac{\partial^4 w_2}{\partial x^4} + \rho A \frac{\partial^2}{\partial t^2} (w_2 - (e_0 a)^2 \frac{\partial^2 w_2}{\partial x^2}) = c(w_1 - w_2) - k_w w_2 \quad (2)$$

Here w_1 and w_2 are flexural displacements of nanoribbons 1 and 2 in the y direction, A is the cross sectional area of each GNR, ρ is the density, I is the moment of inertia, E is the Young's modulus, a is the C-C bond length and e_0 is a parameter representing nonlocal elastic effects in the GNR^{56,57}. Without loss of generality, we consider a simplified case with $e_0a = 0$ and $k_w = c$ ⁵⁶, and use the parameters obtained in Ref⁵⁶. The two governing equations (Eqs. 1 and 2) can then be written in the form $L\vec{u}=0$ where $\vec{u} = \begin{pmatrix} w_1 \\ w_2 \end{pmatrix}$, and L is a linear operator.

Solutions of the form $\vec{u} = \begin{pmatrix} D_{w_1} \\ D_{w_2} \end{pmatrix} \exp i(\beta x - \omega t)$ are assumed, where D_{w_1} and D_{w_2} are the corresponding magnitudes of w_1 and w_2 , and β and ω are the wavenumber and the angular frequency of the propagating wave. The corresponding solution results in two vibrational modes as shown in Fig 1(b). Mode 1 corresponds to the in-phase mode with $D_{w_1}^{(1)} = D_{w_2}^{(1)}$ and mode 2 corresponds to the anti-phase mode with $D_{w_1}^{(2)} = -D_{w_2}^{(2)}$. We note that below the cut-off frequency, f_c , only the in-phase branch exists, see Fig. 1(b). The value of the cut-off frequency depends on the nanoribbon and elastic matrix properties⁵⁶, $f_c = \frac{1}{2\pi} \sqrt{\frac{k_w + 2c}{\rho A}}$, which in this system is around 20.5 THz for nanoribbons of 4 nm width⁵⁶.

Clearly, the dispersion curves plotted in Fig. 1(b) are symmetric with respect to wavenumber β , implying that the wave propagation in such a waveguide is reciprocal, i.e. waves traveling in forward and backward directions have the same properties. In order to break this symmetry in the wave propagation phenomenon we follow the technique suggested in Refs^{46,53}. In particular, we consider wave propagation with a spatio-temporally modulated elastic matrix. In this case we expect that for an appropriately chosen modulation, one-way conversion between the guided modes may be induced, i.e. interaction between the guided waves is possible in one propagation direction only.

We assume spatio-temporal modulation of the elastic matrix constant so that $k_w = k_{w0} + \delta k_w \cos(\Omega t - Bx)$ where k_{w0} is the original stiffness constant and δk_w is the modulation depth. In order to maximize the coupling between modes, we modulate only the upper elastic matrix, as shown in Fig. 2. To solve the governing equations for the modulated system, we assume a general solution as the superposition of the guided modes:

$\vec{u}' = a_1(x) \begin{pmatrix} D_{w_1}^{(1)} \\ D_{w_1}^{(1)} \end{pmatrix} \exp i(\beta_1 x - \omega_1 t) + a_2(x) \begin{pmatrix} D_{w_1}^{(2)} \\ -D_{w_1}^{(2)} \end{pmatrix} \exp i(\beta_2 x - \omega_2 t)$, where $\beta_{1,2}$ and $\omega_{1,2}$ are the wavevectors and frequencies of in-phase and anti-phase modes, and $a_1(x)$ and $a_2(x)$ are their slowly varying spatial amplitudes. Next, using the standard techniques of the perturbation theory, two ordinary differential equations are obtained.

$$\frac{d}{dx} \begin{pmatrix} a_1 \\ a_2 \end{pmatrix} = \begin{pmatrix} 0 & i\xi_1 \exp(-i\beta'x) \\ i\xi_2 \exp(i\beta'x) & 0 \end{pmatrix} \begin{pmatrix} a_1 \\ a_2 \end{pmatrix} \tag{3}$$

where $\xi_1 = \frac{\delta k_w}{16EI\beta_1^3}$, $\xi_2 = \frac{\delta k_w}{16EI\beta_2^3}$, and $\beta' = \beta_2 - \beta_1 - B$. Based on the incoming signal frequency ω_1 and the available modulation frequency Ω , a full mode conversion from mode 1 to mode 2 occurs when $\omega_2 = \omega_1 + \Omega$ and when the B parameter of the modulation is chosen such that $B = \beta_2 - \beta_1$ or $\beta' = 0$. In this case, under phase-matching conditions, the differential equations can be simplified to

$$\frac{d^2}{dx^2} \begin{pmatrix} a_1 \\ a_2 \end{pmatrix} = \begin{pmatrix} -A_{11} & 0 \\ 0 & -A_{22} \end{pmatrix} \begin{pmatrix} a_1 \\ a_2 \end{pmatrix} \tag{4}$$

where $A_{11} = A_{22} = \frac{\delta k_w^2}{256(EI)^2 \beta_1^3 \beta_2^3}$. The system shows one-way behavior because the modulation $k_w = k_{w0} + \delta k_w \cos(\Omega t - Bx)$ does not convert the mode at $(-\beta_1, \omega_1)$ to any other modes. The resulting end point of the intended transition in the negative β region does not lie on the anti-phase branch of the dispersion curve (Fig. 1(b)). This one-way behavior arises because the modulation breaks both time-reversal and spatial-inversion symmetry.

If we consider the propagation of the in-phase mode in the system, the initial conditions will be $a_1(0) = 1$ and $a_2(0) = 0$. The solution to equation 4 is then written as $a_1(x) = \cos(\xi x)$ and $a_2(x) = \sin(\xi x)$, where ξ is the conversion wavevector. As described in Fig. 3(a), complete transition from in-phase to anti-phase mode is observed for the wave propagating in one direction (solid lines), while in the opposite direction the in-phase mode will not be influenced (dashed lines). The general solution of the governing equations is then

$\cos(\xi x) \begin{pmatrix} D_{w_1}^{(1)} \\ D_{w_1}^{(1)} \end{pmatrix} \exp i(\beta_1 x - \omega_1 t) + \sin(\xi x) \begin{pmatrix} D_{w_1}^{(2)} \\ -D_{w_1}^{(2)} \end{pmatrix} \exp i(\beta_2 x - \omega_2 t)$ with $\xi = \frac{\delta k_w}{16EI\sqrt{\beta_1^3 \beta_2^3}}$, and the corresponding conversion length of $l_c = \frac{\pi}{2\xi} = \frac{8\pi EI\sqrt{\beta_1^3 \beta_2^3}}{\delta k_w}$. As expected, the conversion length is inversely

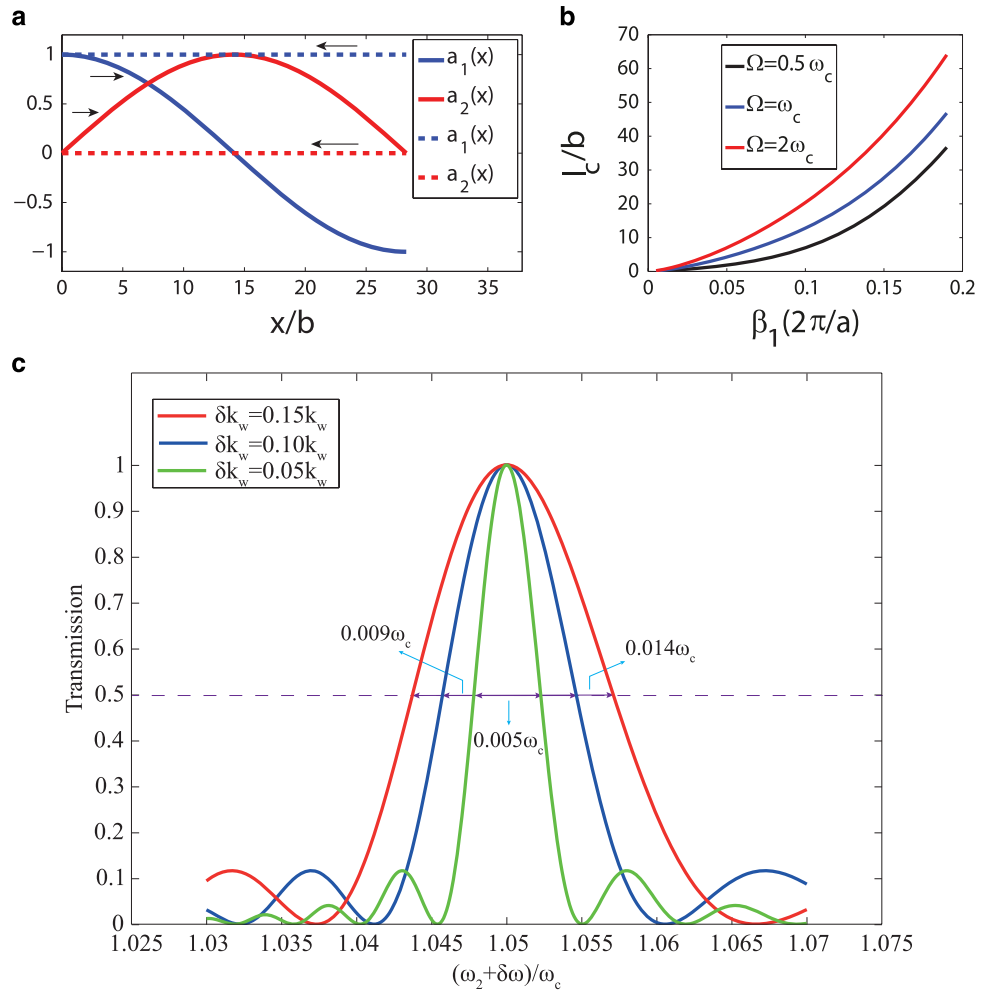


Figure 3. (a) Variation of mode amplitudes along the modulation domain. As shown by the arrows, the solid lines correspond to forward propagation with full conversion and the dashed lines correspond to backward propagation with no mode conversion. (b) Conversion length for different values of Ω as a function of wave number of in-phase mode. (c) Transmission coefficient of mode 2 calculated for different operational frequencies. The red, blue, and green curves correspond to different modulation depths at $\delta k_w = 0.15k_w$, $\delta k_w = 0.1k_w$, and $\delta k_w = 0.05k_w$, respectively. The bandwidths shown in the figure are determined by considering the frequency span for which the transmission coefficient drops by 50%.

proportional to the modulation depth. This means that with stronger modulation, the mode conversion requires a smaller modulation domain. To analyze the conversion length further, we investigate its dependence on the modulation parameters. The intent of adding a modulation domain is to convert an incoming in-phase mode signal with frequency ω_1 and wavenumber β_1 to the anti-phase mode using the available modulation frequency Ω and tunable modulation wavenumber B . Therefore, we plot the dependence of the conversion length on wavenumber β_1 for different values of Ω . As shown in Fig. 3(b), the required conversion length is larger for higher wavenumbers, as l_c varies proportional to $(\beta_1\beta_2)^{\frac{3}{2}}$ with $\beta_2 = \left[(\rho A (\Omega + \sqrt{\frac{EI\beta_1^4 - k_w}{\rho A}})^2 + k_w + 2c) / (EI) \right]^{\frac{1}{4}}$. It is worth mentioning that the choice of Ω and β_1 is not arbitrary and should satisfy two criteria. First, the corresponding mode 1 frequency, ω_1 , needs to be below the cut-off frequency. Second, the resulting frequency value $\Omega + \omega_1$ needs to lie on the dispersion curve of mode 2 in the forward propagation direction (positive β side) and lie on a band gap region in the backward propagation direction (negative β side) consistent with Fig. 1(b).

As an example, we choose a value slightly below the cut-off frequency to guarantee that at frequency ω_1 the system only supports the in-phase mode. For $\omega_1 = 0.95\omega_c$, $\Omega = 0.1\omega_c$ and $\delta k_w = 0.1k_w$, $l_c = 34.6\lambda_1$ where $\lambda_1 = \frac{2\pi}{\beta_1}$ is the wavelength of the corresponding mode 1 signal. Here we use normalized quantities in both the analytical and the numerical calculations. The corresponding wavelength of mode 2 based

on the dispersion curves will be $\omega_2=1.05\omega_c$. It is important to emphasize that the parameter values chosen are arbitrary and longer wavelength signals corresponding to smaller choices of ω_1 can also be used to observe the same isolation effect as long as the required conditions explained earlier are satisfied. Additionally, lower values of the modulation depth also result in a mode conversion, but require a longer modulation domain. Furthermore, the operational bandwidth is also important in evaluating the performance of the isolator. In order to estimate the bandwidth of the system operation depending on the modulation length, we have calculated the transmission characteristics of our system analytically. Typically, the outgoing signal can be a combination of mode 1 and mode 2 signals as described by the spatially varying mode amplitudes, $a_1(x)$ and $a_2(x)$, shown in Fig. 3(a). In the general case where a phase-mismatch could be present, the spatially varying amplitudes are given as

$$a_1(x) = \exp(-ix\beta'/2) \left[\cos(x\sqrt{\xi_1\xi_2 + (\beta'/2)^2}) + i\frac{\beta'/2}{\sqrt{\xi_1\xi_2 + (\beta'/2)^2}} \sin(x\sqrt{\xi_1\xi_2 + (\beta'/2)^2}) \right] \quad \text{and}$$

$$a_2(x) = i \exp(ix\beta'/2) \frac{\xi_2}{\sqrt{\xi_1\xi_2 + (\beta'/2)^2}} \sin(x\sqrt{\xi_1\xi_2 + (\beta'/2)^2}), \text{ where } \beta' \text{ measures the phase mismatch}$$

introduced when the operational frequency ω_1 is changed by a small value, $\delta\omega$. Since the modulation frequency and length are fixed, the frequency of the converted mode ω_2 is also changed by the same value. The transmission coefficient of the converted mode can be calculated based on

$$T=1 - \left| \cos(l_c\sqrt{\xi_1\xi_2 + (\beta'/2)^2}) + i\frac{\beta'/2}{\sqrt{\xi_1\xi_2 + (\beta'/2)^2}} \sin(l_c\sqrt{\xi_1\xi_2 + (\beta'/2)^2}) \right|^2. \text{ The resulting transmission}$$

coefficients are shown in Fig. 3(c) for a system with $\Omega=0.1\omega_c$, $\omega_1=0.95\omega_c$, and with different modulation depths of $\delta k_w=0.15k_w$, $\delta k_w=0.1k_w$, and $\delta k_w=0.05k_w$, which correspond to modulation lengths of around $24\lambda_1$, $35\lambda_1$ and $71\lambda_1$ respectively. As shown in Fig. 3(c), the transmission coefficient drops fairly rapidly as the frequency is changed. This drop occurs because, due to the shape of the dispersion curves, the spatial modulation B is no longer commensurate with the difference between the wavenumbers of modes 2 and 1 at $\omega_2 + \delta\omega$ and $\omega_1 + \delta\omega$. The corresponding bandwidth was calculated by considering a frequency span at which the transmission coefficient drops by 50%. For the three cases studied here shown by the red, blue, and green curves, the bandwidth is around $0.014\omega_c$, $0.009\omega_c$, and $0.005\omega_c$ respectively. The results show that in order to have a larger operational bandwidth, a larger modulation depth needs to be provided.

In order to confirm the analytical model, we used numerical simulations of the wave propagation and mode conversion in double-layer GNRs using the finite difference time-domain (FDTD) method to solve the governing equations in the presence of spatio-temporal modulation. For this purpose, we choose a modulation domain with length l_c as predicted from the analytical model. The numerical simulation results are shown in Fig. 4. An incoming in-phase wave of wavelength λ_1 will be converted to an anti-phase wave of wavelength λ_2 after passing through the modulation domain. The Fourier spectra of both the incoming and outgoing signals are shown in Fig. 4(b). From the FDTD simulations, the peak corresponding to the frequency of the outgoing signal (red curve) is around $\omega_2=1.08\omega_1$ which shows good agreement with the analytical method. The design of the system provides conversion of a signal of mode 1 to a signal of mode 2 in only one of the propagation directions. Therefore, in the opposite direction where no conversion between the two modes happens, we essentially observe a transmission ratio of 1 for the signal. In the other direction the signal of mode 1 is converted to mode 2 which implies a transmission ratio of close to zero. In fact, qualitatively, this type of isolation results in the following scattering matrix for the two ports: $\begin{pmatrix} 0 & 0 \\ 1 & 0 \end{pmatrix}$. More specifically, if we consider the Fourier spectrum of the outgoing signal in Fig. 4(b), a transmission ratio of slightly above zero is observed for the forward propagation direction. However, this value of transmission ratio is influenced by the numerical errors within the framework of the FDTD method and it is important to keep in mind that the analytical method suggests a transmission ratio of zero for this scenario.

Experimental realization of spatio-temporal modulation of elastic properties has been investigated recently. Spatial property modulation is possible through periodic arrangement of elastic material similar to the case of phononic crystals⁵⁹. Temporal property modulation, although more difficult, is also possible in practice through applying electric fields, magnetic fields or mechanical strains in a periodic fashion^{60–62}. In general, spatial modulations with nanometer scale periodicity provide suitable conditions for conversion between the two vibrational modes of double-layer GNRs. Furthermore, THz range frequencies are appropriate for temporal modulations to guarantee the unidirectional nature of such systems. Beyond double-layer GNRs, the aforementioned technique is also applicable to other systems. The key here is to have a system with two different branches of dispersion curve separated by a cut-off frequency. Using the same method, one-way mode conversion is achievable in systems such as single layer GNRs or double-wall carbon nanotubes where similar types of governing equations describe their behavior^{56,63–66}. It is also important to mention that for very short wavelength limits the physics of the problem may differ from the predictions of continuum models and therefore atomistic level techniques such as molecular dynamics simulations⁶⁷ may be required for the analysis.

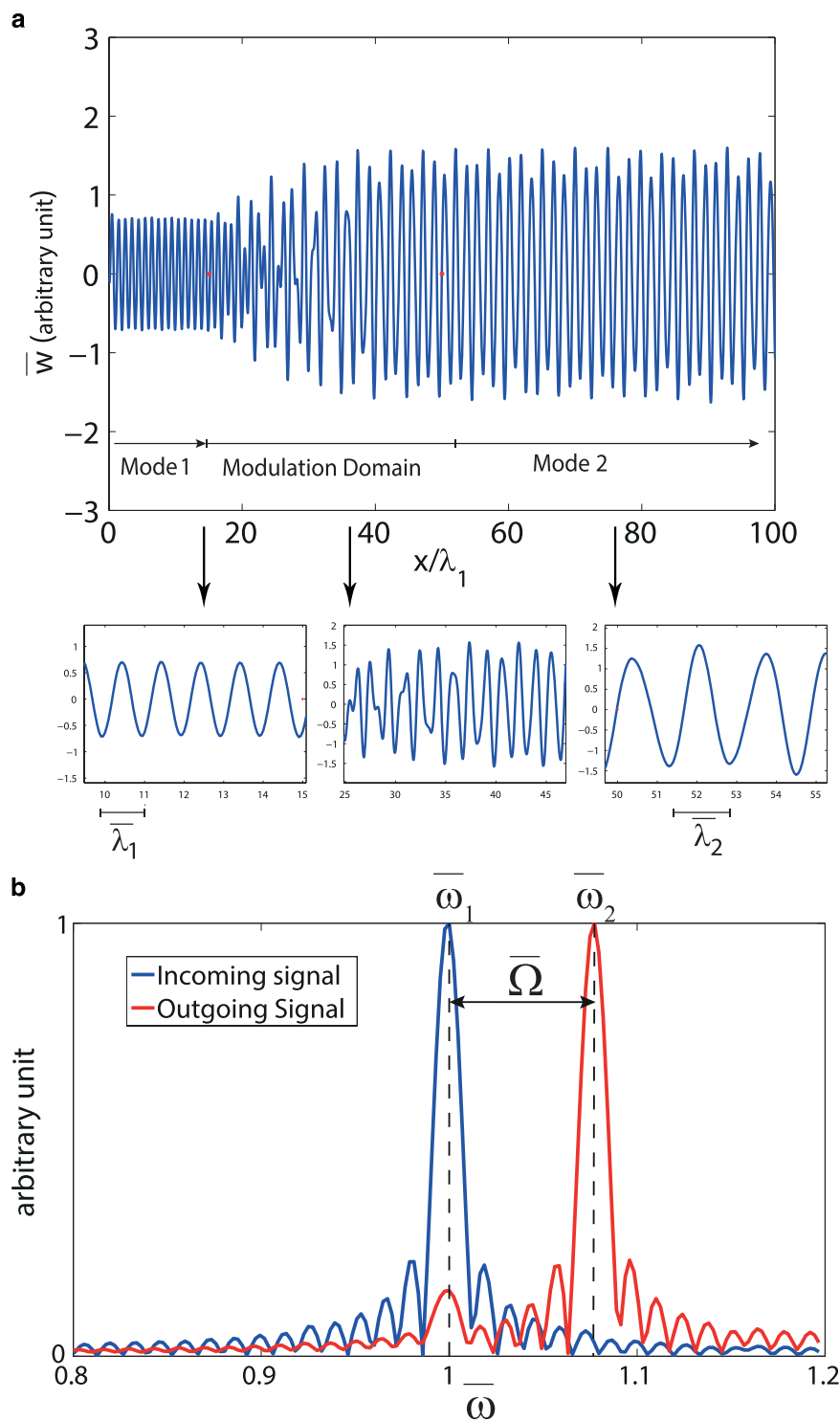


Figure 4. (a) FDTD simulation of in-phase to anti-phase mode conversion in double-layer graphene nanoribbons. x is scaled with respect to $\lambda_1 = \frac{2\pi}{\beta_1}$. (b) Fourier spectrum of the signal before and after the modulation domain. The horizontal axis is normalized with respect to the frequency of mode 1. The blue curve shows the Fourier transform of mode 1 which is peaked at a value of 1 corresponding to $\bar{\omega}_1$. The red curve is the Fourier transform of the signal after the modulation domain which shows a peak at $\bar{\omega}_2=1.08$.

In this paper, we explored one-way acoustic signal isolation in graphene nanoribbons. We showed that through spatio-temporal modulation of the system properties, we can convert a signal of one mode to another mode in one direction, while no conversion is observed in the opposite direction. Combined with appropriate mode filters that filter out signals of frequency ω_2 , a signal of frequency ω_1 can be

absorbed or filtered out after conversion to a signal of frequency ω_2 in one propagation direction while it will be transmitted with no disturbance as the same signal with frequency ω_1 in the opposite direction. This method is not limited to graphene nanoribbons and can be used to induce the same type of signal isolation for acoustic wave propagation in other low dimensional oscillators. The realization of a NEMS based signal isolators raises intriguing possibilities for a wide range of applications in scanning probe microscopes, force and displacement detection devices and chemical and biological sensors.

References

- Novoselov, K. S. *et al.* Electric field effect in atomically thin carbon films. *Science* **306**, 666 (2004).
- Geim, A. K. & Novoselov, K. S. The rise of graphene. *Nat. Mater.* **6**, 183 (2007).
- Meyer, J. C. *et al.* The structure of suspended graphene sheets. *Nature* **446**, 60 (2007).
- Jia, X. *et al.* Controlled formation of sharp zigzag and armchair edges in graphitic nanoribbons. *Science* **323**, 1701 (2000).
- Bethune, D. S. *et al.* Cobalt-catalysed growth of carbon nanotubes with single-atomic-layer walls. *Nature* **363**, 605 (1993).
- Chopra, N. G. *et al.* Boron nitride nanotubes. *Science* **269**, 966 (1995).
- Chen, Z.-G. *et al.* Novel boron nitride hollow nanoribbons. *Science* **2**, 2183 (2008).
- Chen, Y. J., Zhang, H. Z. & Chen, Y. Pure boron nitride nanowires produced from boron triiodide. *Nanotechnology*. **17**, 786 (2006).
- Suryavanshi, A. P., Yu, M.-F., Wen, J., Tang, C. & Bando, Y. Elastic modulus and resonance behavior of boron nitride nanotubes. *Appl. Phys. Lett.* **84**, 2527 (2004).
- Mak, K. F., Lee, C., Hone, J., Shan, J. & Heinz, T. F. Atomically thin MoS₂: A new direct-gap semiconductor. *Phys. Rev. Lett.* **105**, 136805 (2010).
- Zhang, Y., Tan, Y.-W., Stormer, H. L. & Kim, P. Experimental observation of the quantum Hall effect and Berry's phase in graphene. *Nature* **438**, 201 (2005).
- Wakabayashi, K., Takane, Y. & Sigrist, M. Perfectly conducting channel and universality crossover in disordered graphene nanoribbons. *Phys. Rev. Lett.* **99**, 036601 (2007).
- Vakil, A. & Engheta, N. Transformation optics using graphene. *Science* **332**, 1291 (2011).
- Liu, M. *et al.* A graphene-based broadband optical modulator. *Nature* **474**, 64 (2011).
- Ghosh, S. *et al.* Dimensional crossover of thermal transport in few-layer graphene. *Nat. Mater.* **9**, 555 (2010).
- Balandin, A. A. *et al.* Superior thermal conductivity of single-layer graphene. *Nano Lett.* **8**, 902 (2008).
- Li, D. & Kaner, R. B. Graphene-based materials. *Science* **320**, 1170 (2008).
- Lee, C., Wei, X., Kysar, J. W. & Hone, J. Measurement of the elastic properties and intrinsic strength of monolayer graphene. *Science* **321**, 1170 (2008).
- Tang, Q. & Zhou, Z. Graphene-analogous low-dimensional materials. *Progress in Materials Science* **58**, 1244 (2013).
- Rueckes, T. *et al.* Carbon nanotube-based nonvolatile random access memory for molecular computing. *Science* **289**, 94 (2000).
- Jang, J. E. *et al.* Nanoscale memory cell based on a nanoelectromechanical switched capacitor. *Nature Nanotechnol.* **3**, 26 (2008).
- Stutzel, E. U. *et al.* A graphene nanoribbon memory cell. *Small* **6**, 2822 (2010).
- Begliarbekov, M., Strauf, S. & Search, C. P. Quantum inductance and high frequency oscillators in graphene nanoribbons. *Nanotechnology* **22**, 165203 (2011).
- Bunch, J. S. *et al.* Electromechanical resonators from graphene sheets. *Science* **315**, 490 (2007).
- Chen, C. *et al.* Performance of monolayer graphene nanomechanical resonators with electrical readout. *Nat. Nanotechnol.* **4**, 861 (2009).
- Garcia-Sanchez, D. *et al.* Imaging mechanical vibrations in suspended graphene sheets. *Nano Lett.* **8**, 1399 (2008).
- Scarpa, F., Chowdhury, R., Kam, K., Adhikari, S. & Ruzzene, M. Dynamics of mechanical waves in periodic graphene nanoribbon assemblies. *Nanoscale Research Lett.* **6**, 430 (2011).
- Craighead, H. G. Nanoelectromechanical systems. *Science* **290**, 1532 (2000).
- Verbridge, S. S., Shapiro, D. F., Craighead, H. G. & Parpia, J. M. Macroscopic tuning of nanomechanics: substrate bending for reversible control of frequency and quality factor of nanostring resonators. *Nano Lett.* **7**, 1728 (2007).
- Papadakis, S. J. *et al.* Resonant oscillators with carbon-nanotube torsion springs. *Phys. Rev. Lett.* **93**, 146101 (2004).
- Ilic, B., Krylov, S. & Craighead, H. G. Theoretical and experimental investigation of optically driven nanoelectromechanical oscillators. *J. Appl. Phys.* **107**, 034311 (2010).
- Verbridge, S. S., Bellan, L. M., Parpia, J. M. & Craighead, H. G. Optically driven resonance of nanoscale flexural oscillators in liquid. *Nano Lett.* **6**, 2109 (2006).
- Forsen, E. *et al.* Ultrasensitive mass sensor fully integrated with complementary metal-oxide-semiconductor circuitry. *Appl. Phys. Lett.* **87**, 043507 (2005).
- Vlaminck, I. D. *et al.* Detection of nanomechanical motion by evanescent light wave coupling. *Appl. Phys. Lett.* **90**, 233116 (2007).
- Mamin, H. J. & Rugar, D. Sub-attoneutron force detection at millikelvin temperatures. *Appl. Phys. Lett.* **79**, 3358 (2001).
- Knobel, R. G. & Cleland, A. N. Nanometre-scale displacement sensing using a single electron transistor. *Nature (London)* **424**, 291 (2003).
- Yaralioglu, G. G., Atalar, A., Manalis, S. R. & Quate, C. F. Analysis and design of an interdigital cantilever as a displacement sensor. *J. Appl. Phys.* **83**, 7405 (1998).
- Manalis, S. R., Minne, S. C., Atalar, A. & Quate, C. F. Interdigital cantilevers for atomic force microscopy. *Appl. Phys. Lett.* **69**, 3944 (1996).
- Ilic, B. *et al.* Enumeration of DNA molecules bound to a nanomechanical oscillator. *Nano Lett.* **5**, 925 (2005).
- Ilic, B. *et al.* Mechanical resonant immunospecific biological detector. *Appl. Phys. Lett.* **77**, 450 (2000).
- Liang, B., Guo, X. S., Tu, J., Zhang, D. & Cheng, J. C. An acoustic rectifier. *Nat. Mater.* **9**, 989 (2010).
- Boechler, N., Theocharis, G. & Daraio, C. Bifurcation-based acoustic switching and rectification. *Nat. Mater.* **10**, 665 (2011).
- Tanaka, Y., Murai, T. & Nishiguchi, N. Rectification of elastic waves in a thin plate. *J. Appl. Phys.* **111**, 024507 (2012).
- Liang, B., Yuan, B. & Cheng, J. C. Acoustic diode: Rectification of acoustic energy flux in one-dimensional systems. *Phys. Rev. Lett.* **103**, 104301 (2009).
- He, Z. J. *et al.* Asymmetric acoustic gratings. *Appl. Phys. Lett.* **98**, 083505 (2011).
- Zanjani, M. B., Davoyan, A. R., Mahmoud, A. M., Engheta, N. & Lukes, J. R. One-way phonon isolation in acoustic waveguides. *Appl. Phys. Lett.* **104**, 081905 (2014).
- Gu, X., Lin, Z., Liang, B., Cheng, J. & Zhang, D. Modeling and optimization of an acoustic diode based on micro-bubble nonlinearity. *J. Acoust. Soc. Am.* **133**, 1119–1125 (2013).
- Li, X. F. *et al.* Tunable unidirectional sound propagation through a sonic-crystal-based acoustic diode. *Phys. Rev. Lett.* **106**, 084301 (2011).

49. Fleury, R., Sounas, D. L., Sieck, C. F., Haberman, M. R. & Alu, A. Sound isolation and giant linear nonreciprocity in a compact acoustic circulator. *Science* **343**, 516 (2014).
50. Popa, B.-I. & Cummer, S. A. Non-reciprocal and highly nonlinear active acoustic metamaterials. *Nat. Comm.* **5**, 3398 (2014).
51. Hafezi, M. & Rabl, P. Optomechanically induced non-reciprocity in microring resonators. *Opt. Express* **20**, 7672 (2012).
52. Lenferink, E. J., Wei, G. & Stern, N. P. Coherent optical non-reciprocity in axisymmetric resonators. *Opt. Express* **22**, 16099 (2014).
53. Yu, Z. & Fan, S. Complete optical isolation by indirect interband photonic transition. *Nat. Photonics* **3**, 91 (2009).
54. Lira, H., Yu, Z., Fan, S. & Lipson, M. Electrically driven nonreciprocity induced by interband photonic transition on a silicon chip. *Phys. Rev. Lett.* **109**, 033901 (2012).
55. Mürmu, T. & Pradhan, S. C. Vibration analysis of nano-single-layered graphene sheets embedded in elastic medium based on nonlocal elasticity theory. *J. Appl. Phys.* **105**, 064319 (2009).
56. Shi, J., Ni, Q., Li, X. & Natsuki, T. Wave propagation in embedded double-layer graphene nanoribbons as electromechanical oscillators. *J. Appl. Phys.* **110**, 084321 (2011).
57. Allegri, G., Scarpa, F., Chowdhury, R. & Adhikari, S. Wave propagation in periodically supported nanoribbons: A nonlocal elasticity approach. *J. Vibration and Acoustics* **135**, 041017 (2013).
58. Senalp, A. D., Arikoglu, A., Ozkol, I. & Dogan, V. Z. Dynamic response of a finite length euler-bernoulli beam on linear and nonlinear viscoelastic foundations to a concentrated moving force. *J. Mech. Sci. Technol.* **24**, 1957 (2010).
59. Hopkins, P. E. *et al.* Reduction in the thermal conductivity of single crystalline silicon by phononic crystal patterning. *Nano Lett.* **11**, 107 (2011).
60. Casadei, F., Delpero, T., Bergamini, A., Ermanni, P. & Ruzzene, M. Piezoelectric resonator arrays for tunable acoustic waveguides and metamaterials. *J. Appl. Phys.* **112**, 064902 (2012).
61. Cullen, J. R., Rinaldi, S. & Blessing, G. V. Elastic versus magnetoelastic anisotropy in rare earth iron alloy. *J. Appl. Phys.* **49**, 1960 (1978).
62. Jang, J.-H., Ullal, C. K., Gorishnyy, T., Tsukruk, V. V. & Thoma, E. L. Mechanically tunable three-dimensional elastomeric network/air structures via interference lithography. *Nano Lett.* **6**, 740 (2006).
63. Bhaskar, A. Elastic waves in Timoshenko beams: the 'lost and found' of an eigenmode. *Proc. R. Soc. A* **465**, 239 (2009).
64. Yoon, J., Ru, C. Q. & Mioduchowski, A. Vibration of an embedded multiwall carbon nanotube. *Compos. Sci. Technol.* **63**, 1533 (2003).
65. Wang, Q. Wave propagation in carbon nanotubes via nonlocal continuum mechanics. *J. Appl. Phys.* **98**, 124301 (2005).
66. Natsuki, T., Hayashi, T., & Endo, M. Wave propagation of carbon nanotubes embedded in an elastic medium. *J. Appl. Phys.* **97**, 044307 (2005).
67. Allen, M. P. & Tildesley, D. J. *Computer Simulation of Liquids* (Oxford Science Publication 2001).

Acknowledgements

This work was supported by the National Science Foundation (Grant No. DMR-1120901)

Author Contributions

M.B.Z. and A.R.D. performed the analytical and numerical calculations. J.R.L. and N.E. supervised the research. The manuscript was written through contributions of all authors.

Additional Information

Competing financial interests: The authors declare no competing financial interests.

How to cite this article: Zanjani, M. B. *et al.* NEMS With Broken T Symmetry: Graphene Based Unidirectional Acoustic Transmission Lines. *Sci. Rep.* **5**, 9926; doi: 10.1038/srep09926 (2015).



This work is licensed under a Creative Commons Attribution 4.0 International License. The images or other third party material in this article are included in the article's Creative Commons license, unless indicated otherwise in the credit line; if the material is not included under the Creative Commons license, users will need to obtain permission from the license holder to reproduce the material. To view a copy of this license, visit <http://creativecommons.org/licenses/by/4.0/>